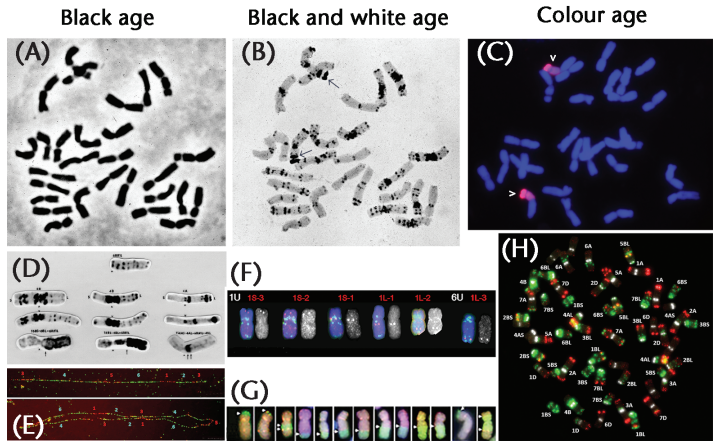

Plate 2.1. The advances in chromosome staining and *in situ* hybridisation methods greatly facilitated chromosome manipulation and crop improvement. (**A**) Conventionally stained *T. durum* mitotic metaphase chromosomes show similar chromosome size and arm ratios and thus individual chromosome identification is impossible (black age). (**B**) The same cell after C-banding (Gill and Kimber 1974; Gill *et al.* 1991), which produces a pattern of dark (heterochromatic) and light (euchromatic) bands along the chromosomes that is chromosome-specific and allows identification of individual chromosomes (black and white age). Note the C-banding identified the wheat–rye whole arm translocation T1RS·1BL (marked by arrows) in this line conferring resistance to leaf, stripe, stem rust, powdery mildew and also has a heterotic effect on grain yield because it also confers a large root mass. (**C**) Genomic *in situ* hybridisation (GISH) of the T1RS·1BL durum germplasm using total genomic rye DNA as a probe labelled with rhodamine together with an excess amount of unlabelled genomic wheat DNA; note the rye chromosome arm is detected by red fluorescence (marked by arrowheads), whereas wheat chromosomes are counterstained with DAPI and fluoresce blue (colour age). C-banding and GISH are powerful methods for monitoring alien chromatin in wide hybridisation. (**D**) C-banding and GISH patterns of radiation-induced terminal and interstitial wheat–rye translocations conferring resistance to Hessian fly, *H21*: T6BS·6BL-6RL, T4BS·4BL-6RL, Ti4AS·4AL-6RL-4AL documenting the amount and position of introduced rye chromatin in wheat chromosomes. Source: Friebe *et al.* (1996), fig. 29. (**E**) Fibre-fluorescence *in situ* hybridisation (Fibre FISH) images of extrachromosomal circular DNA molecules (eccDNAs) in glyphosate-resistant *Amaranthus palmeri*; **upper insert:** linear form of eccDNA; **lower insert:** dimerised circular form of eccDNA with head-to tail tandem orientation (#1, BAC 01G15; #2, BAC 13C09; #3, BAC 22F22; #4, BAC 23A10; #5, BAC 03A06; #6, BAC 08H14). Source: Koo *et al.* (2018), fig. 2b, c). Fibre FISH can visualise naked DNA molecules, the above experiment demonstrated novel eccDNA molecules controlling a glyphosate resistant trait. (**F**) Single-gene FISH patterns using homoeologous group-1 probes to mitotic metaphase chromosomes of *Aegilops umbellulata*; note that the 1L-3 probe hybridises to a distal region of the group-6 *Ae. umbellulata* chromosome, indicating the presence of an interchromosomal translocation. Source: Danilova *et al.* (2014), fig. 4b). Single-gene FISH allows rapid determination of gene synteny, which is the first necessary first step in alien introgression. (**G**) GISH analysis of introgression library of alien chromatin from chromosome 5M^g (labelled green) of *Aegilops geniculata* into wheat chromosome 5D (red). (**H**) Identification of wheat B-genome telocentric chromosomes using multicolor FISH probed with CL191 (red), GAAn (green) and CRWs (white), note that the FISH signals of CL191 were located in telomeric regions of 2BL, 3BL, 7BL and 7BS, whereas the signals for CRWs were located in the centromeric region of all the B-genome telosomes except 1BS and 6BS. Source: Koo *et al.* (2016), fig. 2b).

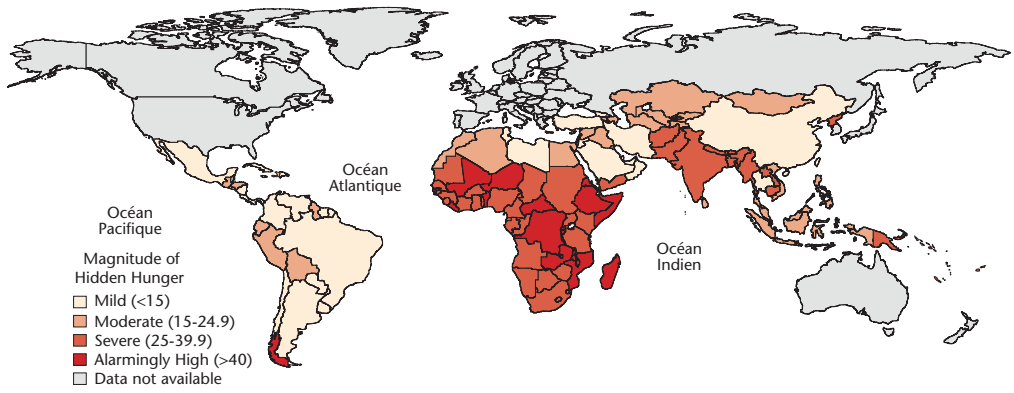

Plate 5.1. Hidden hunger index, 2011. Source: Ruel-Bergeron *et al.* (2015), CC BY 4.0.

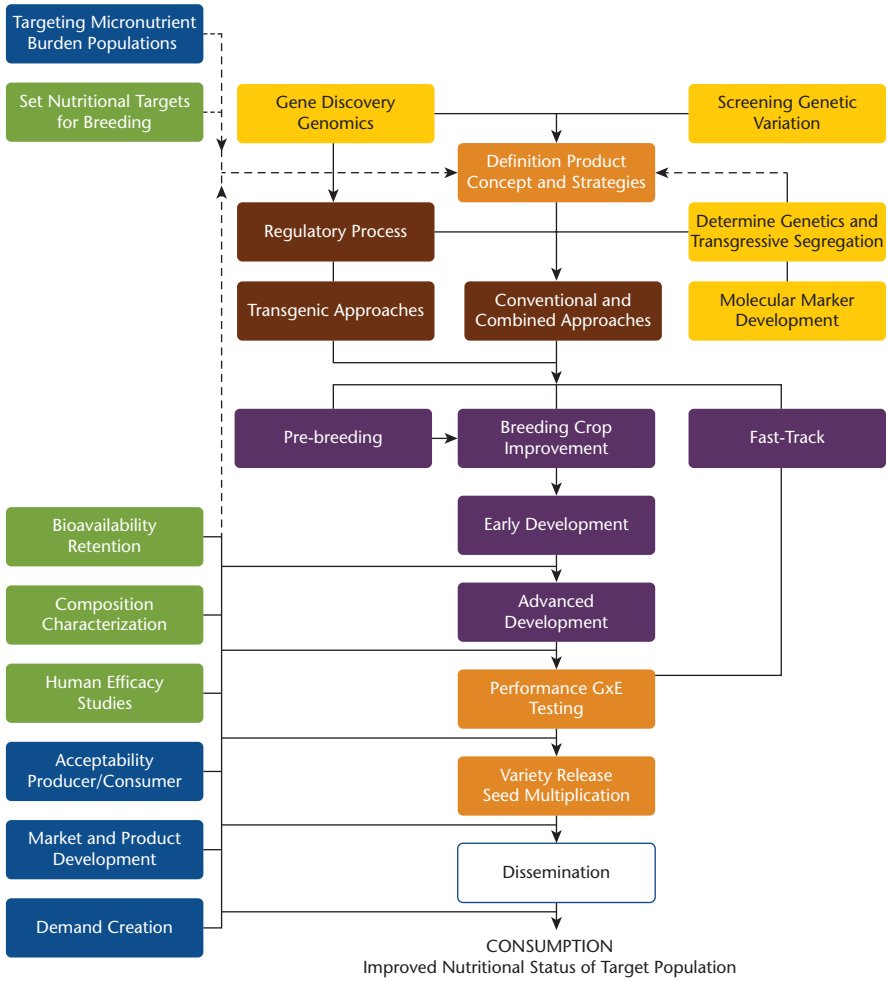

Plate 5.2. Crop development framework. Source: Bouis and Saltzman (2017a), CC BY 4.0.

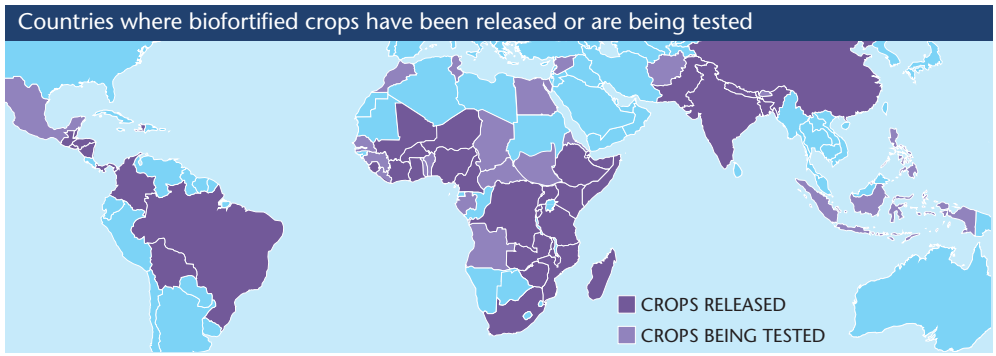

Plate 5.3. Biofortified crop map (January 2017). Biofortified crops have been released in countries indicated in dark purple, while crops are being tested in countries in light purple. This map includes countries where the International Potato Center (CIP) has worked to release the orange sweet potato. More detailed information about the varieties tested and released in each country is given in Bouis and Saltzman (2017b, Chapter 5). Source: Bouis and Saltzman (2017a), CC BY 4.0.

Plate 12.1. Two-dimensional projection of a point cloud of dormant grapevines acquired with a full waveform LiDAR (photograph courtesy of Alex Held, CSIRO; funded by the National Collaborative Research Infrastructure Strategy TERN initiative). **(A)** The 'Echidna' LiDAR is a tripod-based device firing LiDAR pulses in a single plane (graphically illustrated in red) while rotating 360 degrees, acquiring spatial information for each return, creating a 3D point cloud; **(B)** this can be viewed as a projection.

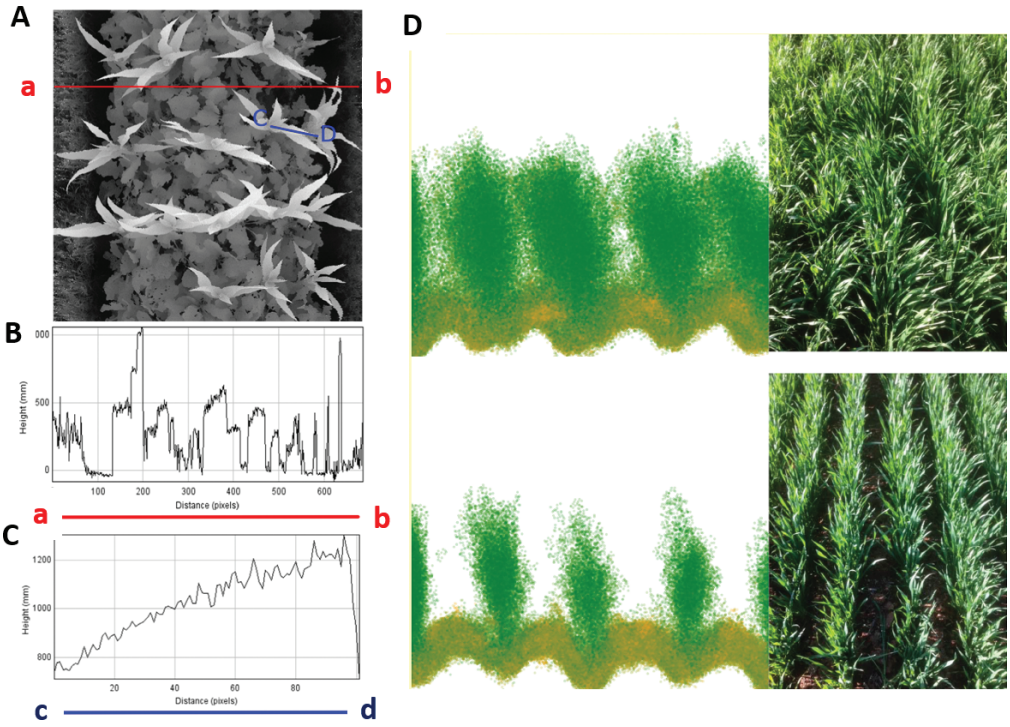

Plate 12.2. LiDAR data of crops acquired with the Phenolite buggy (Jimenez-Berni *et al.* 2018) using a discrete LiDAR mounted at the nadir angle above the canopy. **Panel A** shows a 2D projection of a LiDAR point cloud generated from a mixed canopy of maize and brassica where the grey scale of the image indicates distance from the sensor (black distal, white proximal). The height profile for the transect of the crop marked a to b is shown in **panel B** while the leaf angle of the maize leaf marked c to d is shown in **panel C** (Jimenez-Berni, Deery, Sirault and Furbank, unpublished). **Panel D**; left panels show a rendering of point clouds of two wheat varieties (erect and prostrate) acquired using the same system and on the right, colour images of the corresponding canopies are shown. Source: Adapted from Rebetzke *et al.* (2016).

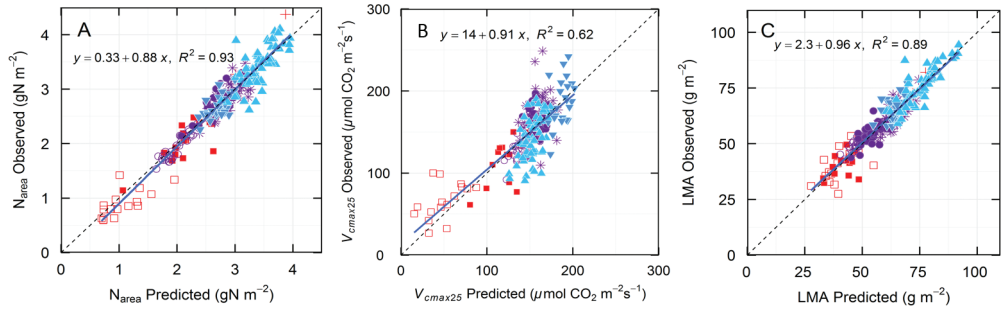

Plate 12.3. Examples of the output of predictive hyperspectral models for: **(A)** wheat leaf nitrogen content; **(B)** Vcmax, a modelled parameter indicative of Rubisco content and **(C)** leaf mass. Partial least-squares regression was used to generate a spectral model based on calibration data acquired by destructive or traditional low throughput techniques and then applied to leaf spectra to predict traits. Source: based on data from Silva-Perez *et al.* (2018).

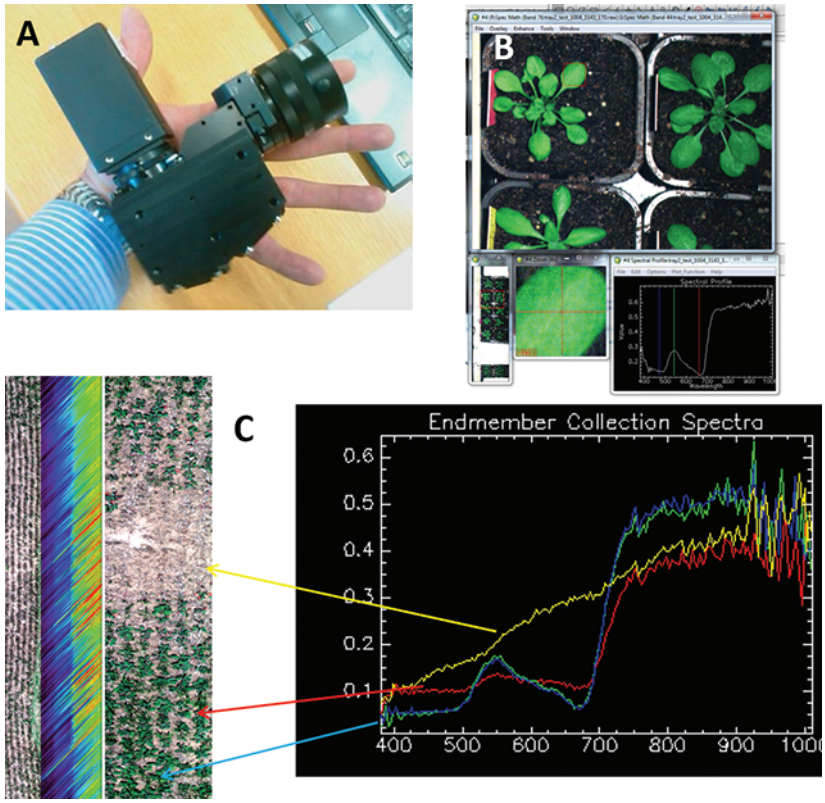

Plate 12.4. **(A)** An image of a Headwall micro-vis/NIR hyperspectral linescanner illustrating the compact dimensions of the instrument. **(B)** Colour images of a tray of *Arabidopsis* generated using the vis/NIR scanner above and an example of a spectrum extracted from a pixel of this spectral data cube of an *Arabidopsis* leaf. **(C)** Similar data generated from a field plot of brassica using the same instrument mounted on the Phenolite, comparing spectra of bare ground and leaf material. Source: Jimenez-Berni *et al.* (2018).

(A)

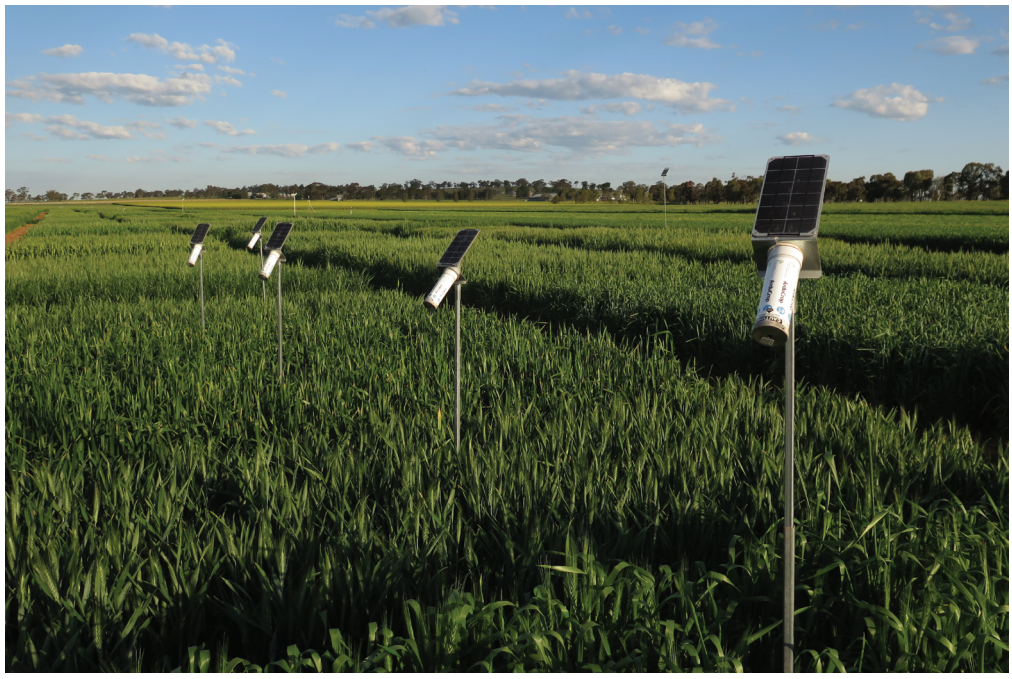

(B)

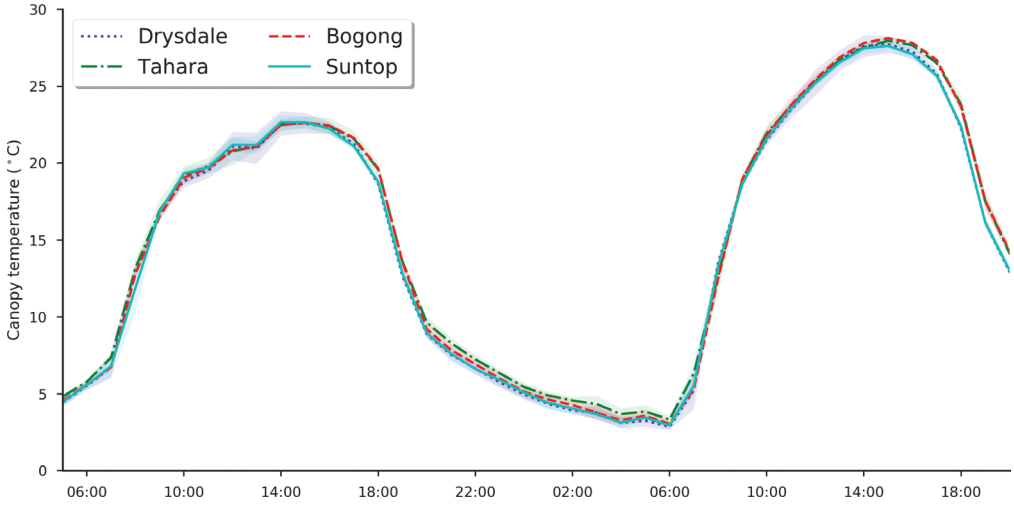

Plate 12.5. **(A)** 'Arducrop' canopy temperature sensors deployed on wheat field trials. **(B)** An example of data collected over a period of 2 days for six replicate plots of six different wheat varieties (standard errors are shown). (Deery, Jimenez-Berni and Furbank, High Resolution Plant Phenomics Centre, CSIRO, unpublished).

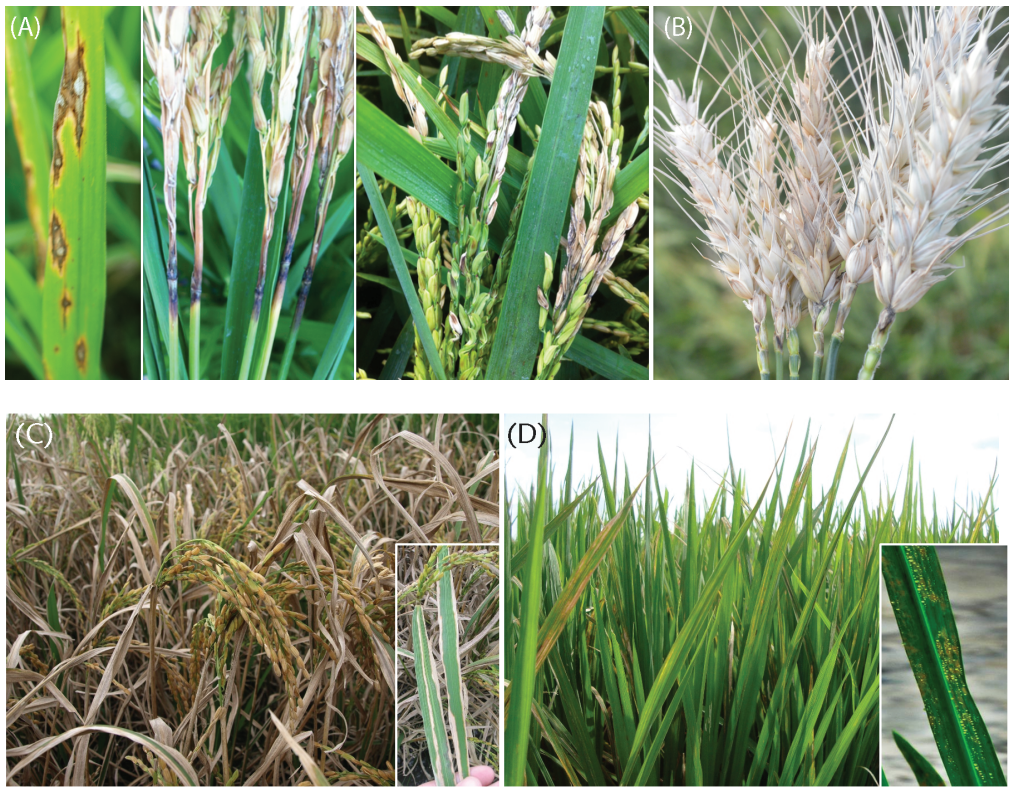

Plate 16.1. *M. oryzae* and *X. oryzae* disease symptoms. **(A)** Rice blast symptoms (*M. oryzae Oryza* pathotype) occur on all above ground parts of the plant. Shown from left to right are leaf blast, neck blast and panicle blast. Sources: Barbara Valent (Kansas State University) for leaf blast and Yeshi Wamishe (University of Arkansas) for neck and panicle blast. **(B)** Symptoms of wheat blast (*M. oryzae Triticum* pathotype) occur mainly on heads in the field. Infection of the rachis (shown) causes death and bleaching of all spikelets above the infection point. Source: Guillermo Isidoro Barea Vargas (Coperagro SRL, Bolivia). **(C)** Symptoms of bacterial blight of rice (*X. oryzae* pv. *oryzae*). Plants in an advanced stage of bacterial blight infection show straw-coloured leaves. The inset shows typical wavy elongated lesions. Source: Modified from Vera Cruz *et al.* (2017). **(D)** Rice plants showing symptoms of bacterial leaf streak, *X. oryzae* pv. *oryzicola* in the field. The inset shows yellow bacterial exudates on a leaf. Source: Modified from Vera Cruz *et al.* (2017).

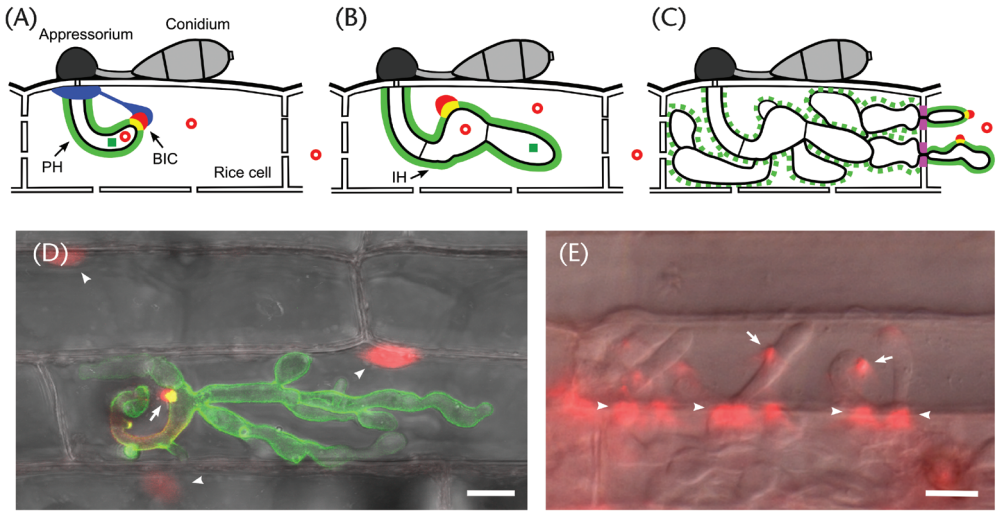

Plate 16.2. Mechanisms underpinning effector triggered susceptibility (ETS), effector triggered immunity (ETI) and PAMP triggered immunity (PTI) in rice. This plate comprises schematic diagrams and supporting live-cell micrographs of *M. oryzae* secreting effector proteins while invading living rice cells (Giraldo and Valent 2013). To cause disease, the fungus continuously colonises living rice cells while delivering apoplastic effectors around host cells and cytoplasmic effectors inside host cells. Sporulating lesions (Plate 16.1A) appear 4 to 5 days later. **(A)** After appressorial penetration, (~22–25 h post inoculation, hpi), the fungus grows as a specialised tubular primary hypha (PH) that is sealed inside a plant-derived extrainvasive-hyphal membrane that separates the hypha from both the rice cytoplasm and the bulk extracellular space. Apoplastic effectors (green squares/line) undergo classical golgi-dependent secretion and remain trapped inside the surrounding plant membrane. In contrast, cytoplasmic effectors (red rings) are secreted using a specialised secretion system, and they accumulate in the biotrophic interfacial complex (BIC, red dome) at the PH hyphal tip before crossing the rice plasma membrane into the cytoplasm (blue). **(B)** At 26–30 hpi, the PH differentiates into bulbous invasive hyphae (IH), and the BIC (red dome) is left behind beside the first IH cell as the IH grow to fill the rice cell. **(C)** At 36–40 hpi, IH form highly constricted pegs to cross the rice cell wall into neighbour cells. The hyphal and BIC development stages repeat for each new hypha that enters a living neighbour cell. **(D)** This confocal microscope projection image shows an IH (at 30 hpi) expressing a green fluorescent apoplastic effector fusion protein (BAS4), and a red fluorescently labelled cytoplasmic effector fusion protein (PWL2) that is also engineered to accumulate in nuclei. Red fluorescent PWL2 accumulated in the BIC (arrow) and in the nuclei of both invaded and uninvaded neighbour cells (arrowheads). Scale bar = 10 µm. **(E)** IH transformed to express a different red fluorescently labelled effector (BAS2) that accumulates at BICs (arrows) and at cell wall crossing points (arrowheads, purple in panel c) at 36 hpi. Scale bar = 10 µm.

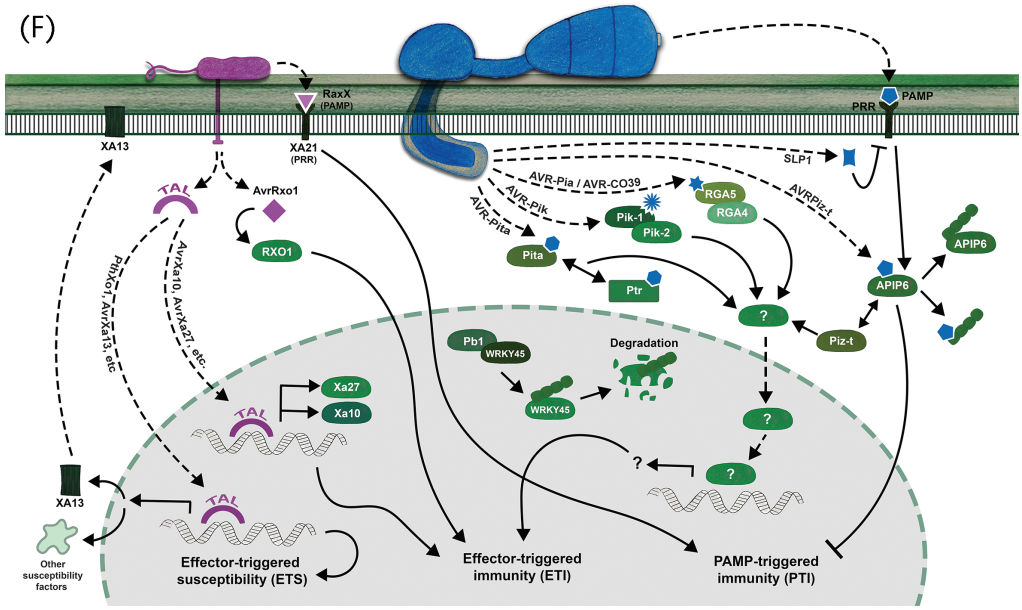

Plate 16.2. Continued. **(F)** Molecular interactions leading to ETS, ETI and PTI (Table 16.1). **(ETS)** *X. oryzae* uses TAL (transcription activator-like) effectors (e.g. avrXa13/pthXo1) to induce ETS by activation of transcription of susceptibility (S) genes, including the SWEET gene *xa13* that encodes a membrane-localised sugar transporter. For *M. oryzae*, apoplastic effector Slp1 promotes susceptibility by inhibiting PTI, specifically by preventing PRR recognition of chitin released from the fungal cell wall. Cytoplasmic effector AvrPiz-t targets a RING finger E3 ligase, APIP6, to modulate rice PTI. The APIP6 and AvrPiz-t proteins are ubiquitinated (green circle chains) as a signal for 26S proteasome-mediated degradation. **(ETI)** Some *X. oryzae* TAL effectors (e.g. avrXa27 and avrXa10) bind to promoters and activate executor genes *Xa27* and *Xa10*. ETI can also be activated by other types of *X. oryzae* effectors (e.g. avrRxo1) through interaction with the NLR protein RXO1. *M. oryzae* AVR effectors trigger ETI through recognition by single NLR receptors (i.e. AVR-Pita or AvrPiz-t), or through recognition by NLR-ID gene pairs (i.e. AVR-Pia/AVR-CO39 or AVR-Pik). One NLR protein, Pb1, promotes ubiquitination of transcription factor WRKY45 and 26S proteasome-mediated degradation leading to ETI. Otherwise, knowledge of downstream events after NLR protein/AVR effector interactions remains limited. **(PTI)** Basal resistance or PTI can be activated by interaction of bacterial or fungal PAMPs with membrane spanning PRRs (pathogen recognition receptors). *Xa21* is a PRR that recognises a sulphated RaxX protein that is conserved in *X. oryzae*. Sources: Plates A–E reproduced with permission from Valent and Khang (2010); Plate 16.2F drawn by Melba Torres Sosa (Colorado State University).

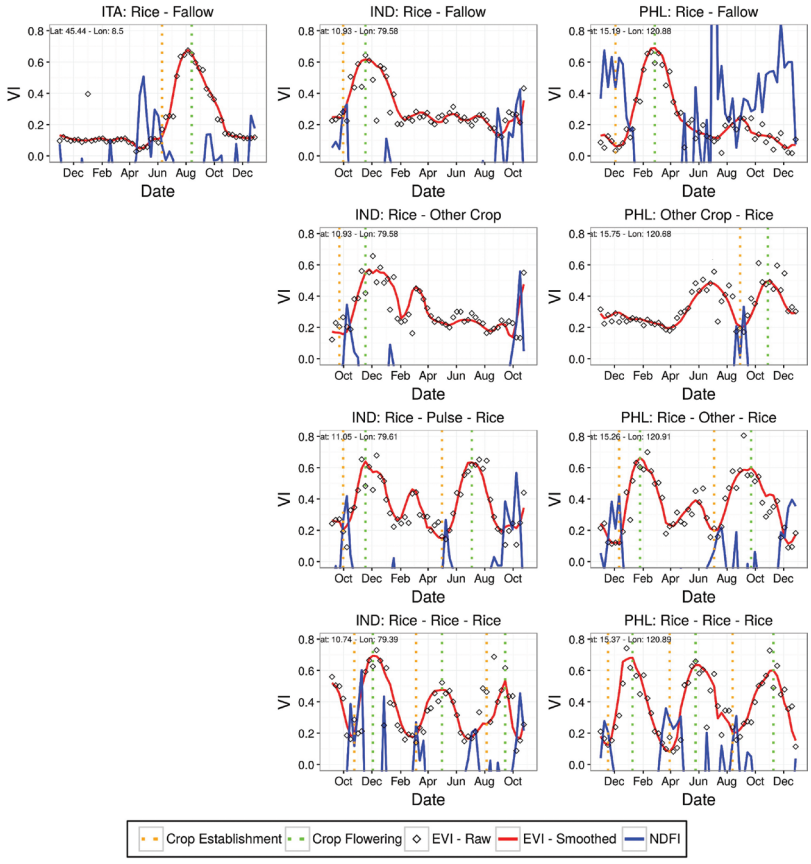

Plate 19.1. The temporal signature of vegetation (original data represented by black circles and the smoothed signal in red) and water (blue) based on MODIS imagery in Italy, India and the Philippines from nine different rice-based systems. Source: Reprinted from Remote Sensing of Environment, Vol 194, Boschetti M, Busetto L, Manfron G, Laborte A, Asilo S, Pazhanivelan S, Nelson A. PhenoRice: A method for automatic extraction of spatio-temporal information on rice crops using satellite data time series, p347–365, doi:10.1016/j.rse.2017.03.029. Copyright (2017), with permission from Elsevier.

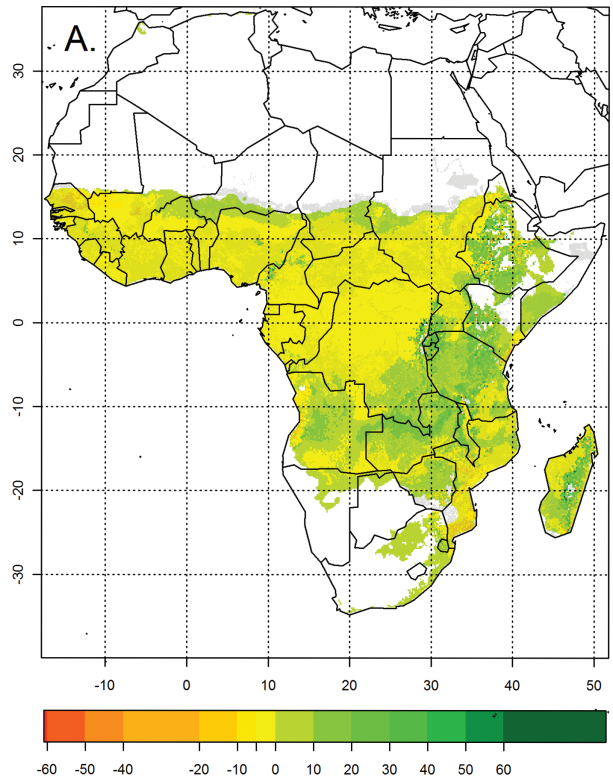

Plate 19.2. Future impact of climate change on cassava suitability in Africa expressed as the percentage change in climate suitability. Areas showing a reduction in suitability are in orange and yellow while areas with increased suitability are green. Suitability is overlaid on croplands in grey. Source: Reprinted by permission from RightsLink Permissions Springer Customer Service Centre GmbH: Springer US, Tropical Plant Biology (https://link.springer.com/journal/12042), Vol 5, Is Cassava the Answer to African Climate Change Adaptation?, Jarvis A, Ramirez-Villegas J, Campo BVH, Navarro-Racines C, p9–29. doi:10.1007/s12042-012-9096-7. Copyright (2012).

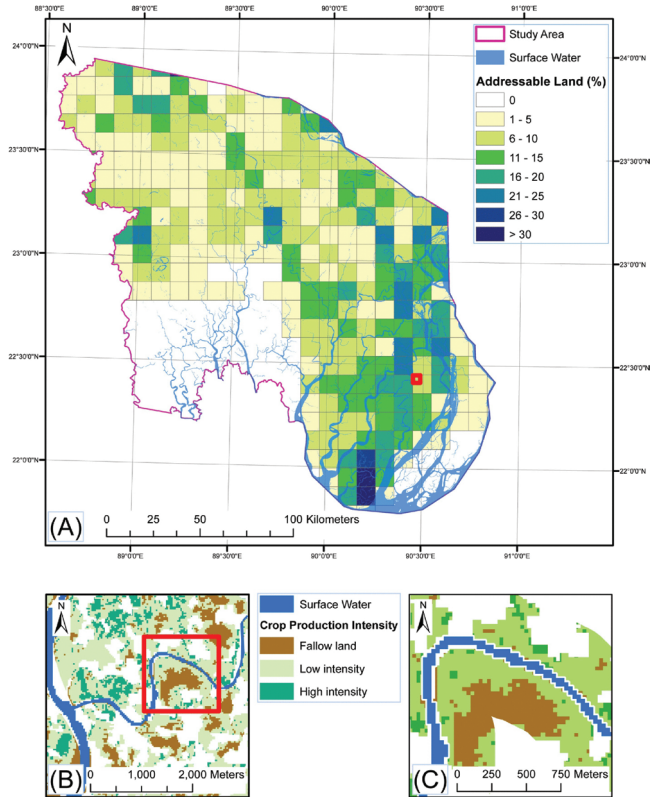

Plate 19.3. **(A)** Agricultural land suitable for surface water irrigation expressed as percentage of total cropland area. **(B)** Detail depicting a block of low-production intensity and fallow land proximal to surface water. **(C)** Further detail depicting a 385 m buffer indicating precise locations of fallow and low-intensity cropland upon which surface water irrigation could be used. Source: Reprinted from Land Use Policy, Vol 60, Krupnik TJ, Schulthess U, Ahmed ZU, McDonald AJ Sustainable crop intensification through surface water irrigation in Bangladesh? A geospatial assessment of landscape-scale production potential, p206–222, doi:10.1016/j.landusepol.2016.10.001, under a Creative Commons Attribution Licence (CC BY) http://creativecommons.org/licenses/by/4.0.

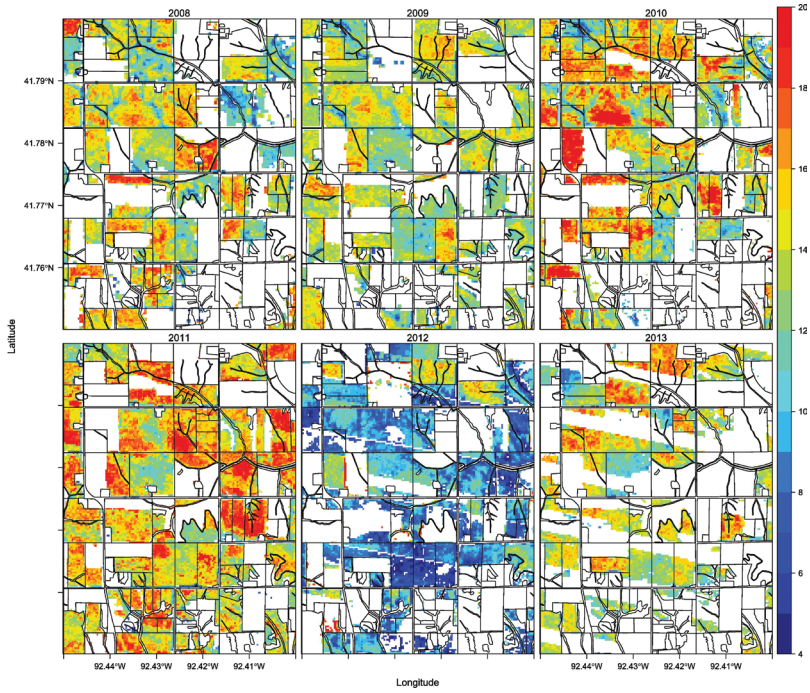

Plate 19.4. High spatial resolution maize yield estimates for 2008–2013 in a part of Poweshiek County, Iowa. Legend shows maize yields in t/ha. Source: Reprinted from Remote Sensing of Environment, Vol 164, Lobell DB, Thau D, Seifert C, Engle E, Little B. A scalable satellite-based crop yield mapper, p324–333, doi:10.1016/j.rse.2015.04.021, Copyright (2015), with permission from Elsevier.

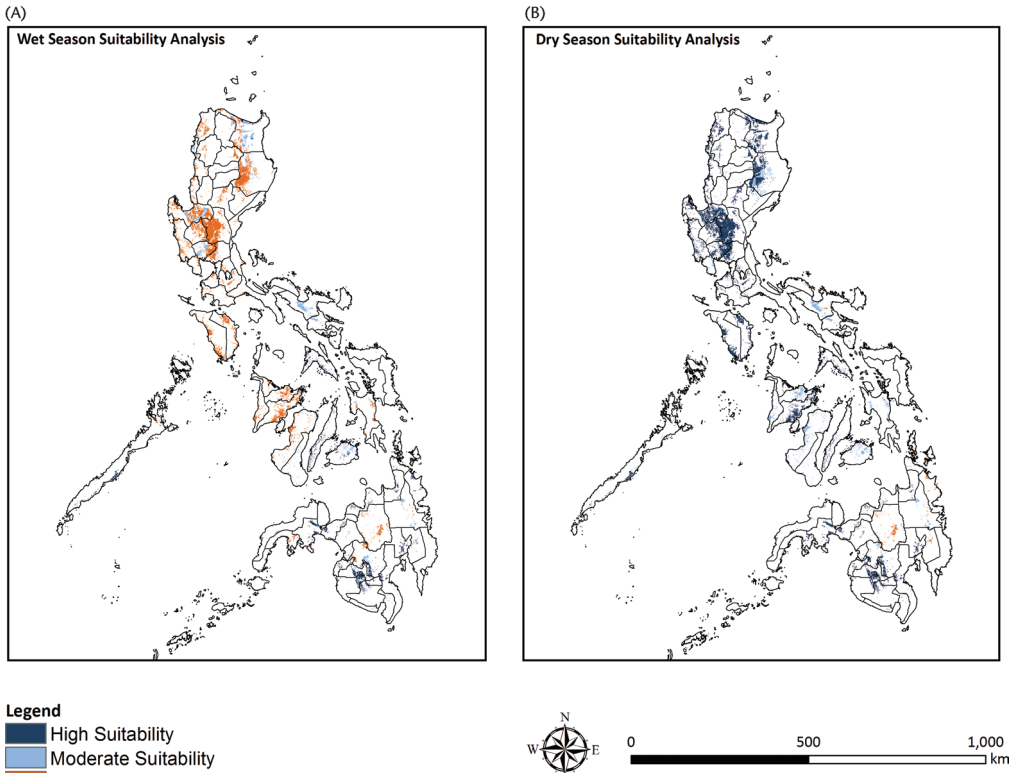

Plate 19.5. The rice growing extent of the Philippines estimated to be climatically suitable for AWD in **(A)** wet harvest season and **(B)** dry harvest seasons in the Philippines. Source: Reprinted from Carbon Management, Vol 8, Sander BO, Wassmann R, Palao LK, Nelson A. Climate-based suitability assessment for alternate wetting and drying water management in the Philippines: a novel approach for mapping methane mitigation potential in rice production, p331–342, doi:10.1080/17583004.2017.1362945, under a Creative Commons Attribution-NonCommercial-NoDerivatives Licence http://creativecommons.org/licenses/by-nc-nd/4.0.

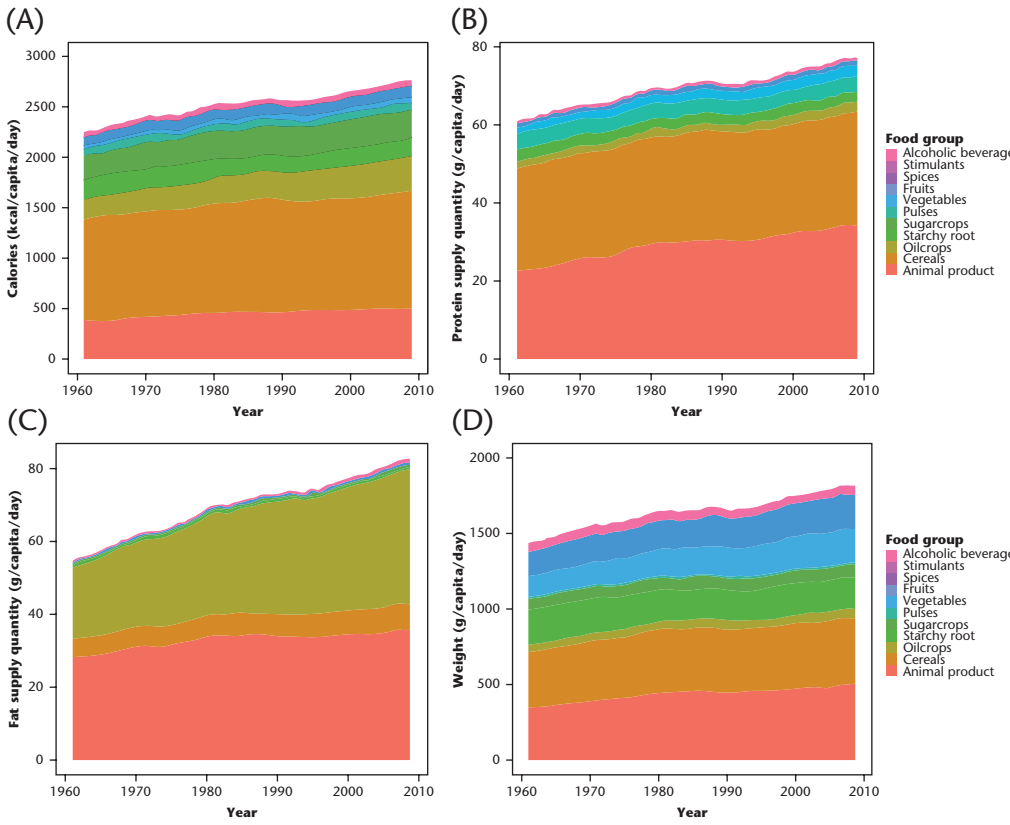

Plate 27.1. Global change in national food supplies of 152 countries by food groups for: **(A)** calories, **(B)** protein, **(C)** fat and **(D)** weight in the period 1961–2009. Source: Reproduced from supplementary information of Khoury *et al.* (2014), with permission of PNAS.